

# On the milling behaviour of flame synthesised titania particles

Casper Lindberg<sup>1</sup>, Jethro Akroyd<sup>1</sup>, Markus Kraft<sup>1,2</sup>

released: 5 December 2016

<sup>1</sup> Department of Chemical Engineering  
and Biotechnology  
University of Cambridge  
New Museums Site  
Pembroke Street  
Cambridge, CB2 3RA  
United Kingdom  
E-mail: [mk306@cam.ac.uk](mailto:mk306@cam.ac.uk)

<sup>2</sup> School of Chemical and  
Biomedical Engineering  
Nanyang Technological University  
62 Nanyang Drive  
Singapore 637459

Preprint No. 177



---

*Keywords:* Titania, population balance, breakage, milling

**Edited by**

Computational Modelling Group  
Department of Chemical Engineering and Biotechnology  
University of Cambridge  
New Museums Site  
Pembroke Street  
Cambridge CB2 3RA  
United Kingdom

**Fax:** + 44 (0)1223 334796

**E-Mail:** [c4e@cam.ac.uk](mailto:c4e@cam.ac.uk)

**World Wide Web:** <http://como.ceb.cam.ac.uk/>

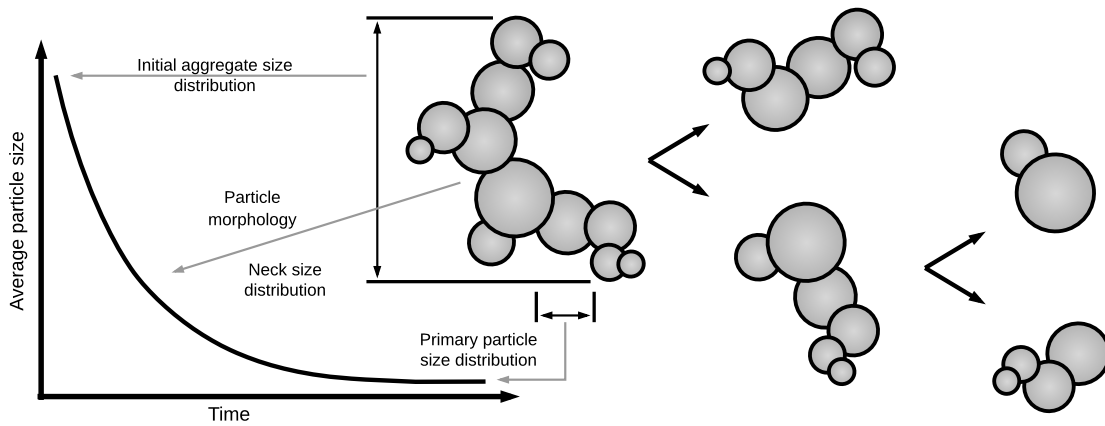


## Highlights

- A laboratory-scale hot wall titania reactor is simulated using a detailed population balance model.
- Breakage models are developed utilising morphological data captured by the detailed particle model.
- The breakage models are used to relate reactor conditions to the milling behaviour of the synthesised titania particles.

## Abstract

A detailed population balance model is used to relate the reactor conditions of flame synthesised titanium dioxide particles to their milling behaviour. Breakage models are developed that utilise morphological data captured by a detailed particle model to relate the structure of aggregate particles to their size-reduction behaviour in the post-synthesis milling process. Simulations of a laboratory-scale hot wall reactor are consistent with experimental data and milling curves predicted by the breakage models exhibit features consistent with experimental observations. The selected breakage model considers the overall fractal structure of the aggregate particles as well as the neck size between neighbouring primary particles. Application of the model to particles produced under different reactor residence times and temperatures demonstrates that the model can be used to relate reactor conditions to the milling performance of  $\text{TiO}_2$  particles.



# Contents

<b>1</b>	<b>Introduction</b>	<b>3</b>
<b>2</b>	<b>Computational details</b>	<b>4</b>
2.1	Particle model . . . . .	5
2.2	Particle processes . . . . .	5
2.2.1	Inception . . . . .	5
2.2.2	Surface growth . . . . .	6
2.2.3	Coagulation . . . . .	6
2.2.4	Sintering . . . . .	6
2.3	Numerical method . . . . .	7
<b>3</b>	<b>Milling models</b>	<b>7</b>
3.1	Neck size calculation . . . . .	8
3.2	Breakage models . . . . .	10
3.2.1	Simple neck model . . . . .	11
3.2.2	Total mass model . . . . .	11
3.2.3	Fragment mass model . . . . .	12
3.2.4	Fragment radius model . . . . .	12
3.2.5	Fragment and neck radius model . . . . .	12
<b>4</b>	<b>Results and discussion</b>	<b>13</b>
4.1	Hot wall reactor simulations . . . . .	13
4.2	Comparison of breakage models . . . . .	16
4.2.1	Milling curves . . . . .	17
4.2.2	Comparison to a first order model . . . . .	19
4.2.3	Choice of breakage model . . . . .	20
4.3	Effect of reactor conditions on milling curves . . . . .	22
<b>5</b>	<b>Conclusions</b>	<b>23</b>
	<b>References</b>	<b>24</b>

# 1 Introduction

Titanium dioxide (titania,  $\text{TiO}_2$ ) particles are an important industrial product. The functionality of the product is strongly influenced by the size, shape, morphology and crystalline phase of the particles. However, we still lack a full understanding of the mechanisms that control the particle properties.

The oxidation of titanium tetrachloride  $\text{TiCl}_4$  is a key route for the industrial manufacture of  $\text{TiO}_2$  particles. The oxidation is typically performed either in a flame or an oxygen plasma. Although the industrial manufacturing process is widely used, optimisation remains largely empirical. In many cases, the product is milled in order to control the final particle size distribution (PSD). This imposes an additional time and energy cost.

Various attempts have been made to understand the flame synthesis of  $\text{TiO}_2$ . Ghoshtagore [18] used a hot-wire experiment to investigate the surface reaction of  $\text{TiCl}_4$  with a  $\text{TiO}_2$  film at 673–1120 K. The reaction was observed to display an Eley-Rideal dependence on  $\text{TiCl}_4$  and  $\text{O}_2$ . The global kinetics of  $\text{TiCl}_4$  oxidation in a hot wall reactor at 973–1273 K was studied by Pratsinis et al. [46]. The reaction was first-order in  $\text{TiCl}_4$  and approximately zero-order in  $\text{O}_2$  up to ten-fold excess  $\text{O}_2$ .

A rate for the gas-phase decomposition of  $\text{TiCl}_4$  was inferred by Pratsinis and Spicer [45] based on the difference between the surface growth rate [18] and the global oxidation rate [46] under the assumption of monodisperse spherical particles. They showed that the surface reaction had a significant effect on the particle diameter. Later studies using more detailed population balance models (PBMs) drew similar conclusions [20, 39, 40, 56].

West et al. [63, 64] proposed a detailed thermodynamically consistent gas-phase kinetic model to describe the oxidation of  $\text{TiCl}_4$ . The main reaction pathway was found to proceed via  $\text{Ti}_2\text{O}_2\text{Cl}_4$ . Unknown thermochemical data were estimated by density functional theory based quantum calculations. Subsequent investigations presented an updated mechanism [65] and considered the role of aluminium trichloride additives [52] and hydrocarbon species [55].

A comparison of the inception behaviour of the mechanisms from Pratsinis and Spicer [45] and West et al. [65] was performed by Mehta et al. [36]. They showed that the choice of model caused inception to occur at different locations in simulations of a turbulent flame. This is consistent with other studies [1, 53]. Mehta et al. [37] subsequently proposed a reduced version of the West et al. [65] mechanism to facilitate the simulation of  $\text{TiCl}_4$  oxidation in turbulent methane flames.

Kraft and co-workers [1, 53] performed a theoretical investigation of the adsorption of  $\text{TiCl}_4$  on the [110] surface of rutile  $\text{TiO}_2$ . Their findings were consistent with an Eley-Rideal surface growth mechanism. The rate parameters of the surface reaction and choice of inception model were observed to strongly affect simulations of Pratsinis' original experiment [46]. The experimental data could be reproduced by simulations using the gas-phase chemistry from West et al. [65] with an inception model based on the collision of any two  $\text{Ti}_x\text{O}_y\text{Cl}_z$  species ( $x, y, z \geq 1$ ). Several surface growth models were proposed based on a combination of the calculated activation energies and fitting to Pratsinis' experiment [46].

Detailed population balance models provide an additional tool to investigate what controls the particle properties [50, 51]. Such models are, within reason, able to include an arbitrarily detailed description of each particle.

This facilitates the simulation of quantities that are directly comparable to experimental observations. For example, size distributions and mass spectra of the particles [12, 34], transmission electron microscopy images and optical band gap measurements [67, 68]. Most importantly, it also enables the option to include key physical details in the model. For example, models where the particle growth is a function of the aggregate composition [10, 11], or, as is the case in this work, where sintering and neck growth are resolved on the basis of individual pairs of neighbouring particles [41, 48, 49, 62]. The level of detail can be reduced once a system is sufficiently well understood. However, Menz and Kraft [38] highlight the pitfalls of using an over-simple model to interpret experimental observations.

Milling has been widely studied due to the high industrial demand for fine powders with tightly controlled properties. A lot of research has focused on identifying optimal milling parameters such as agitation speed, milling media size, filling ratio and suspension concentration. The effect of operational parameters on the milling performance of titanium dioxide has been investigated for fine grinding and dispersion of particles in wet stirred mills [3, 26, 42]. Other work has studied the substructure and mechanical properties of titania agglomerates [17], and the changes in fractal morphology of dense aggregates under wet milling [27].

Population balance models have been used to characterise the milling process and identify breakage mechanisms in wet stirred media milling [5, 21, 22, 58] by fitting Kapur's approximate first order solution [28] to experimental data. More complex models consider non-linear effects and time-variant PBMs [6, 7].

Over long milling times and for sub-micron sized particles more complex phenomena are typically observed. This includes time delays in breakage [7], and grinding limits due to a minimum obtainable particle size and agglomeration effects [16, 22, 26, 54]. Modelling multimodal particle size distributions with statistical laws has been used as an alternative method for obtaining the grinding kinetics [3, 16].

The **purpose of this paper** is to develop a breakage model utilising the morphological data captured by a detailed particle model. This allows us to relate the reactor conditions during particle synthesis to the milling performance of  $\text{TiO}_2$  particles. The particles are simulated using a detailed population balance model that describes the time evolution of the internal structure of the fractal aggregates. The simulation results are post-processed using a breakage model to provide proof of concept that the morphological data in the detailed model can be related to milling behaviour. Five different breakage models are compared.

## 2 Computational details

A detailed population balance model coupled to a gas-phase kinetic model is used to simulate the evolution of the  $\text{TiO}_2$  particles. The kinetic model for the formation of  $\text{TiO}_2$

particles from  $\text{TiCl}_4$  is based on the mechanism proposed by West et al. [65]. It comprises 28 gas-phase species and 66 reactions. The dynamics of the population are described by the Smoluchowski coagulation equation with additional terms for particle inception, surface growth and sintering. The mathematical details of the model and methods are described in detail elsewhere [50], so only a brief summary is given here.

## 2.1 Particle model

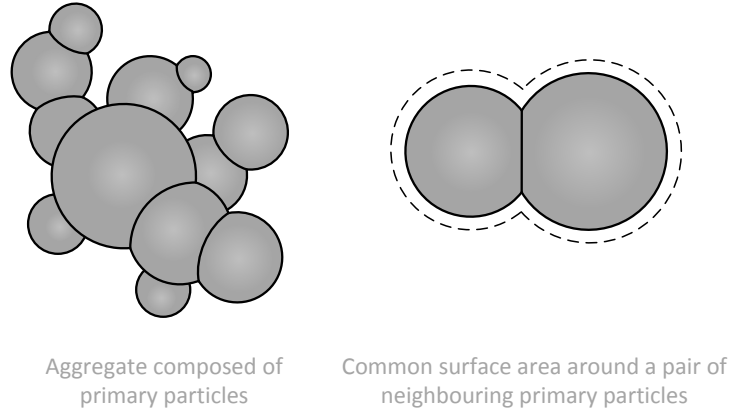


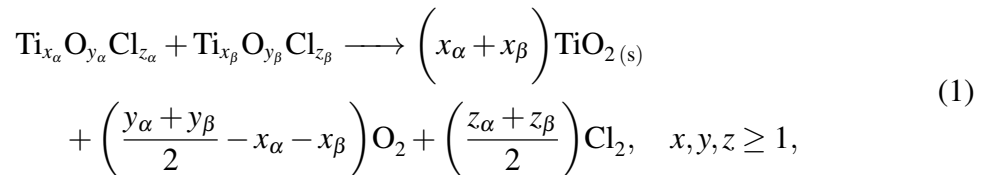
**Figure 1:** Type space of the detailed population balance model.

The description of each aggregate in the population balance model (formally known as the type space) is illustrated in figure 1. Each aggregate is composed of primary particles, where neighbouring particles may be in point contact, fully coalesced or anywhere between. The model resolves the common surface area between each pair of neighbouring primary particles. The primary particle composition of an aggregate is polydispersed where each primary is described in terms of the number of  $\text{TiO}_2$  units, from which the mass and volume are derived.

## 2.2 Particle processes

### 2.2.1 Inception

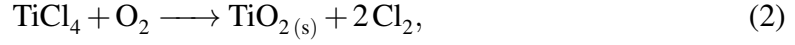
Inception, modelled as per Akroyd et al. [1], is assumed to be collision-limited and result from the bimolecular collision of gas-phase titanium oxychloride species



where the molecular collision diameter is taken as 0.65 nm [65]. An inception event creates a particle consisting of a single primary composed of  $(x_\alpha + x_\beta)$   $\text{TiO}_2$  units.

### 2.2.2 Surface growth

Surface growth is treated as a single-step reaction as in Akroyd et al. [1]



with the rate expression

$$\frac{d[\text{TiO}_2]}{dt} = k_s A_s [\text{TiCl}_4] [\text{O}_2], \quad (3)$$

where  $A_s$  is the surface area per unit volume of the  $\text{TiO}_2$  population and  $k_s$  has an Arrhenius form

$$k_s = A \exp\left(\frac{-E_a}{RT}\right) \frac{\text{m}}{\text{s}} \cdot \frac{\text{m}^3}{\text{mol}}, \quad (4)$$

with activation energy  $E_a$  and pre-exponential factor  $A$ . One surface growth event adds one unit of  $\text{TiO}_2$  to the particle. Equation (3) assumes fixed reaction orders with respect to  $\text{TiCl}_4$  and  $\text{O}_2$ . Alternative models for the rate of surface growth are discussed by Shirley et al. [53].

### 2.2.3 Coagulation

An aggregate is formed when two particles stick together following a collision. The rate of collision is calculated using the transition regime coagulation kernel [44]. After a coagulation event, two primary particles (one from each coagulating particle) are assumed to be in point contact.

### 2.2.4 Sintering

Following the approach of Xiong and Pratsinis [66] and West et al. [65], sintering is modelled as occurring between neighbouring pairs of primary particles, where it is assumed that the common surface area  $C$  exponentially decays to the surface area of a mass-equivalent spherical particle,  $S_{\text{sph}}$ ,

$$\frac{dC}{dt} = -\frac{1}{\tau_s} (C - S_{\text{sph}}), \quad (5)$$

where  $\tau_s$  is a characteristic sintering time taken from Kobata et al. [29] as per West et al. [65]. The sintering level of two primaries  $p_i$  and  $p_j$  is defined as per Shekar et al. [50],

$$s(p_i, p_j) = \frac{\frac{S_{\text{sph}}(p_i, p_j)}{C} - 2^{-1/3}}{1 - 2^{-1/3}}. \quad (6)$$

Note that  $0 \leq s(p_i, p_j) \leq 1$ . Primaries are assumed to have coalesced if the sintering level exceeds 0.95. In this case the two primary particles merge into a single primary with the total  $\text{TiO}_2$  composition of the original primaries.



## 2.3 Numerical method

The detailed population balance equations are solved using a stochastic numerical method [50]: a direct simulation algorithm with various enhancements to improve efficiency. The method uses a majorant kernel and fictitious jumps [14, 19, 44] to improve the computational speed of calculating the coagulation rate. A linear process deferment algorithm [43] is used to provide an efficient treatment of sintering and surface growth. Coupling of the particle model to the gas-phase chemistry, solved using an ODE solver, is achieved by an operator splitting technique [9].

## 3 Milling models

In the milling process, particles break due to stresses exerted by the milling media. Kwade et al. [31, 33] describe the process in terms of the frequency of stress events and the intensity of each stress event. The energy intensity is introduced as a key factor in determining whether a breakage event occurs. A stress event of sufficient intensity will result in breakage.

Low intensity shear stresses are sufficient for breaking weak agglomerates whereas higher intensity normal stresses are required to break crystalline material [32]. Normal stresses arise when a particle is caught in between milling beads during a collision. The resulting fragment size distribution is dependent on the properties of the material and the mode of fragmentation.

Three types of breakage mechanism are usually discussed in the literature: abrasion, cleavage and fracture [2, 7, 23, 24, 47, 58]. Abrasion involves a continuous loss of mass from the surface of a particle resulting in a bimodal fragment distribution. Cleavage produces fragments of the same order in size as the original particle while fracture results in disintegration of the particle into small fragments. The different modes of fragmentation often occur simultaneously during milling.

Epstein [15] first introduced population balance equations to the study of milling, modelling breakage as two successive operations represented by a selection and a breakage function. The selection function is the probability of a particle of given size breaking and is usually observed to increase with particle size [24]. The breakage function describes the shape of the fragment size distribution and is characterised by the fragmentation mechanism.

The idea of this work is to explore whether the information in the type space of the detailed population balance model can be related to the observed milling performance of  $\text{TiO}_2$  particles. The particle breakage rate and fragment distribution are determined by a breakage model that utilises the morphological information captured by the detailed particle model.

Figure 2 shows a sketch of a milling curve. The average particle size is observed to decrease during the initial part of the milling curve. Eventually the system reaches an asymptotic state where no further significant decrease is observed.

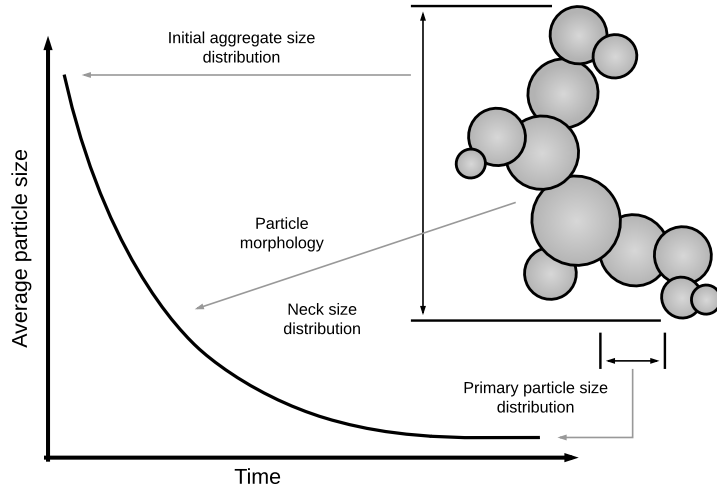


**Figure 2:** *Sketched milling curve related to particle morphology.*

One possible concept relating the detailed particle model to the milling curve is shown overlaying figure 2. The average particle size is obtained from the aggregate size distribution and the asymptotic particle size is a function of the primary particle size distribution. The slope of the milling curve, related to the rate of breakage and fragment distribution, is some function of the aggregate particle structure. Breakage, assumed to occur at the necks between neighbouring primaries, is related to the neck size distribution and the fractal geometry of the particle. The particle geometry is responsible for transmitting milling stresses to necks and the neck strength is related to the neck size.

In this work, we apply a milling model based on algorithm 1 as a post-process to the detailed population balance model. The particle breakage rate is given by the breakage models discussed in section 3.2. Two of the breakage models utilise a neck radius to characterise how strongly neighbouring primaries are connected. The neck model is discussed in the next section.

### 3.1 Neck size calculation

A neck between two primary particles is modelled as overlapping spheres as shown in figure 3. The neck size can be calculated from the common surface area  $C_{ij}$  and spherical-equivalent radii  $r_i$  and  $r_j$  of each primary particle.

The volume  $V$  and surface area  $S$  of two overlapping spheres are given

$$V(R_1, R_2, d) = \frac{4\pi}{3} (R_1^3 + R_2^3) - \frac{\pi}{12d} (R_1 + R_2 - d)^2 (d^2 + 2R_1d + 2R_2d - 3R_1^2 - 3R_2^2 + 6R_1R_2), \quad (7)$$

and

$$S(R_1, R_2, d) = 4\pi (R_1^2 + R_2^2) - \pi (a^2 + H_1^2) - \pi (a^2 + H_2^2), \quad (8)$$

**Algorithm 1:** Milling algorithm applied as a post-process to the detailed particle model.

**Input:** Initial state of the particle ensemble at time  $t_0$ ; Final time  $t_{\text{stop}}$ .

**Output:** State of the particle ensemble at final time  $t_{\text{stop}}$ .

$t \leftarrow t_0$ .

**while**  $t < t_{\text{stop}}$  **do**

Calculate the rate,  $\rho_{\text{part}}(P_q)$ , for each aggregate particle  $P_q$ ,

$$\rho_{\text{part}}(P_q) = \sum_{i < j} \rho_{ij},$$

where  $\rho_{ij}$  is the breakage rate for the neck between two primaries  $p_i$  and  $p_j$ .

Calculate the total rate,  $\rho_{\text{total}}$ , for all  $N$  particles,

$$\rho_{\text{total}} = \sum_{q=1}^N \rho_{\text{part}}(P_q).$$

Calculate an exponentially distributed waiting time  $\Delta t$  with parameter  $\rho_{\text{total}}$ ,

$$\Delta t = \frac{-\ln(X)}{\rho_{\text{total}}},$$

where  $X$  is a uniform random variate in the interval  $[0, 1]$ .

With probability  $\rho_{\text{part}}(P_q)/\rho_{\text{total}}$  select a particle  $P_q$ .

With probability  $\rho_{ij}/\rho_{\text{part}}(P_q)$  select a neck.

Break the neck between primaries  $p_i$  and  $p_j$ , and update the particle ensemble:

$$P_q \rightarrow P_r + P_s,$$

$$N \leftarrow N + 1.$$

Increment  $t \leftarrow t + \Delta t$ .

**end**

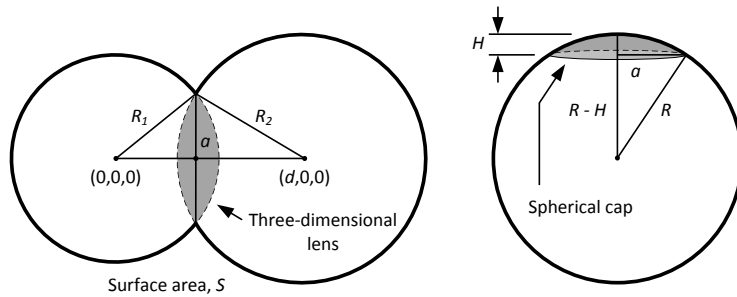


**Figure 3:** Geometry of the neck between two primary particles.

where  $a$  is the radius of the neck [60]

$$a(R_1, R_2, d) = \frac{1}{2d} \left[ (R_1 + R_2 + d)(R_1 + R_2 - d)(-R_1 + R_2 - d)(R_1 - R_2 - d) \right]^{\frac{1}{2}}, \quad (9)$$

and where  $H_1$  and  $H_2$  are the heights of the spherical caps

$$H_i = R_i - R_i \cos \left( \arcsin \left( \frac{a}{R_i} \right) \right),$$

and  $R_1$  and  $R_2$  are the radii of two spheres whose centres are separated by a distance  $d \in [0, R_1 + R_2]$ . The final term in equation (7) is the volume of the three-dimensional lens [60] and the final terms in equation (8) are the areas of each spherical cap [61] created by the intersection of the spheres.

Under the assumption that the volume of the three-dimensional lens is evenly redistributed over the surface of the particles in an even layer of thickness  $\Delta r$ , the radii of each sphere in figure 3 can be written in terms of the spherical-equivalent radii of the corresponding primary particles

$$R_i = r_i + \Delta r. \quad (10)$$

Equations (7) and (8) may be reduced to two equations in two unknowns using the substitutions in equations (9) and (10),

$$\begin{aligned} V(\Delta r, d) &= v(p_i) + v(p_j), \\ S(\Delta r, d) &= C_{ij}, \end{aligned}$$

and can be solved for the values of  $\Delta r$  and  $d$ , and hence the radius of the neck  $a_{ij}(\Delta r, d)$  for each pair of neighbouring primary particles with corresponding total volume  $v(p_i) + v(p_j)$  and common surface area  $C_{ij}$ .

## 3.2 Breakage models

Figure 4 illustrates a single breakage event where an aggregate particle  $P_q$  fragments into two smaller daughter particles  $P_r$  and  $P_s$ . Breakage is treated as binary and always occurs at a neck connecting two neighbouring primary particles. Individual primaries are assumed not to break.

An aggregate particle is modelled as two arms extending from a neck as depicted by the dashed arrows in figure 4. Note that this representation can be applied to any chosen neck within the aggregate. The composition of the arms is equivalent to that of the two daughter fragments formed in the event of breakage. When a particle is caught in a three-body collision with two milling beads the stresses are transmitted by these arms to the neck. The neck that breaks during such a collision will depend on a number of factors including the neck size or strength, and the size, shape and orientation of the respective arms.

The rate of breakage of a neck between two primaries  $p_i$  and  $p_j$  is expressed as a function of the neck and daughter particle (fragment) properties

$$\rho_{ij} = \rho_{ij}(P_r(\dots, p_i, \dots, \mathbf{C}_r), P_s(\dots, p_j, \dots, \mathbf{C}_s), a_{ij}), \quad (11)$$

where  $P_r(\dots, p_i, \dots, \mathbf{C}_r)$  and  $P_s(\dots, p_j, \dots, \mathbf{C}_s)$  are the daughter particles formed in the breakage event,  $a_{ij}$  is the neck radius, and  $\mathbf{C}$  is the respective connectivity matrix storing the

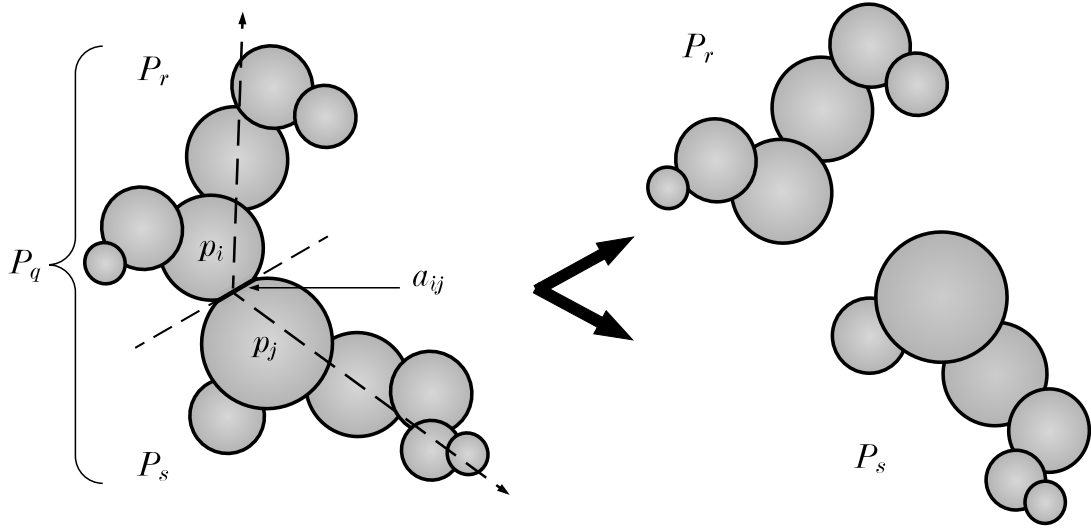


**Figure 4:** A breakage event. An aggregate particle  $P_q$  fragments into two daughter particles  $P_r$  and  $P_s$  at a neck of radius  $a_{ij}$  connecting two primaries  $p_i$  and  $p_j$ . The aggregate is represented as two arms, corresponding to the respective daughter particles, extending from the neck.

common surface areas as defined in Shekar et al. [50]. Five different breakage models are discussed below. It is assumed that a rate constant  $k$  captures the operational parameters of the mill and that the mill is capable of producing collisions of sufficient intensity to break all particle necks. The total particle breakage rate for a particle  $P_q$  is

$$\rho_{\text{part}}(P_q) = \sum_{i < j} \rho_{ij}, \quad (12)$$

where we sum over  $i < j$  to avoid double counting.

### 3.2.1 Simple neck model

The breakage rate is assumed to be only a function of the neck radius, calculated as per section 3.1

$$\rho_{ij} = k a_{ij}^\alpha, \quad (13)$$

for constants  $k$  and  $\alpha$ .

### 3.2.2 Total mass model

The probability of breakage is typically observed to increase with particle size. In this model we assume that the rate of breakage for a neck is proportional to the sum of daughter fragment masses  $m(P_r)$  and  $m(P_s)$  or equivalently, the total particle mass  $m(P_q)$

$$\rho_{ij} = k(m(P_r(\dots, p_i, \dots, \mathbf{C}_r)) + m(P_s(\dots, p_j, \dots, \mathbf{C}_s))) \quad (14)$$

$$= km(P_q(\dots, p_i, p_j, \dots, \mathbf{C}_q)), \quad (15)$$

for constant  $k$ . Breakage is equally likely for every neck in an aggregate. The rate of breakage for a single aggregate particle is therefore a function of its total mass and the number of necks.

$$\rho_{\text{part}}(P_q) = k(n_p(P_q) - 1)m(P_q), \quad (16)$$

where  $n_p(P_q)$  is the number of primaries and  $(n_p(P_q) - 1)$  corresponds to the number of necks, which is always one less than the number of primaries.

### 3.2.3 Fragment mass model

A simple way to characterise the size of a fragment arm is by its mass. More massive arms are expected to apply greater stresses on a neck due to greater leverage and arms of similar mass will maximise the applied stress. This is modelled by setting the rate of breakage proportional to the product of the daughter particle masses

$$\rho_{ij} = k \cdot m(P_r(\dots, p_i, \dots, \mathbf{C}_r)) \cdot m(P_s(\dots, p_j, \dots, \mathbf{C}_s)), \quad (17)$$

for a constant  $k$  and where  $m(P_r)$  and  $m(P_s)$  are the masses of the two particle fragments joined at the neck between primaries  $p_i$  and  $p_j$ .

### 3.2.4 Fragment radius model

A better measure of the size of a fragment arm is its radius of gyration, which accounts for the fractal structure of the aggregate,

$$R_g = \bar{d}_p \left( \frac{n_p}{k_f} \right)^{1/D_f}. \quad (18)$$

$n_p$  is the number of primaries,  $\bar{d}_p$  is the average primary diameter,  $D_f$  is the fractal dimension, and  $k_f$  is the fractal prefactor. A typical value of 1.8 is assumed for the fractal dimension [57]. Using the same form for the rate as in equation (17) the breakage rate for a single neck is

$$\rho_{ij} = k \cdot R_g(P_r(\dots, p_i, \dots, \mathbf{C}_r)) \cdot R_g(P_s(\dots, p_j, \dots, \mathbf{C}_s)), \quad (19)$$

for a constant  $k$  and where  $R_g(P_r)$  and  $R_g(P_s)$  correspond to the radii of gyration of the two arms extending from the neck between primaries  $p_i$  and  $p_j$ .

### 3.2.5 Fragment and neck radius model

The fragment radius of gyration model in section 3.2.4 assumes that all necks are equally strong. However, the degree of sintering between primary particles will effect the breakage rate. By combining the fragment radius model (section 3.2.4) and the simple neck model (section 3.2.1) we can relate the breakage rate to both the geometry of the aggregate particle and the size of the neck. The rate of breakage is

$$\rho_{ij} = k \cdot R_g(P_r(\dots, p_i, \dots, \mathbf{C}_r)) \cdot R_g(P_s(\dots, p_j, \dots, \mathbf{C}_s)) \cdot a_{ij}^\alpha, \quad (20)$$

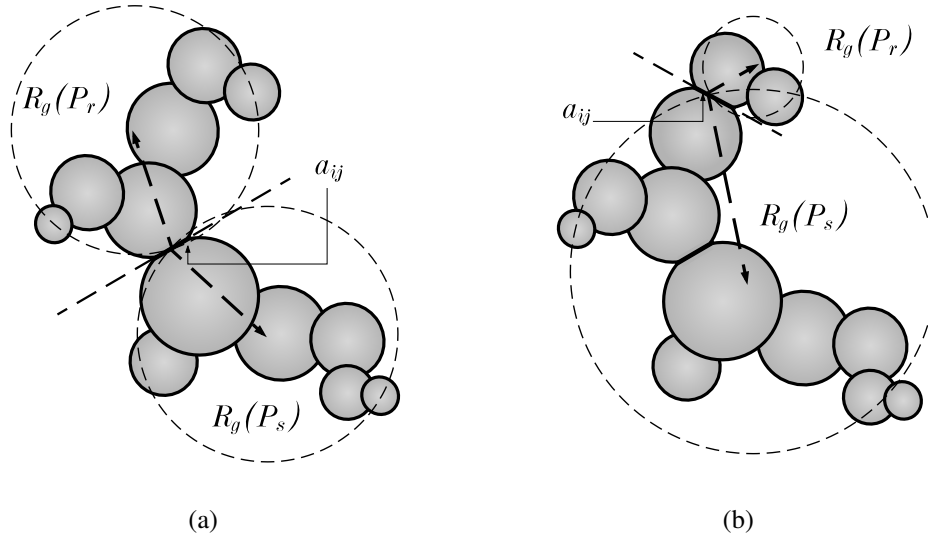


**Figure 5:** Two possible breakage events. The selected neck between primaries  $p_i$  and  $p_j$  is indicated by a dashed line and the fragment arms extending from the neck have radii of gyration  $R_g(P_r)$  and  $R_g(P_s)$ . Symmetrical breakage in subfigure (a) produces daughter fragments with similar radii of gyration while subfigure (b) shows an asymmetrical breakage event.

for constants  $k$  and  $\alpha$ .

Figure 5 illustrates two possible breakage events. We expect that breakage is most likely if both radii of gyration are large and of similar magnitude as shown in figure 5(a). However, in the case of a very weak neck an asymmetrical abrasion-like event is also possible as depicted in figure 5(b).

## 4 Results and discussion

### 4.1 Hot wall reactor simulations

To produce particles for post-processing with the milling models we simulated the hot wall reactor experiment of Pratsinis et al. [46], fitting the surface growth rate for the detailed particle model. The original investigation measured the reaction of 5:1 (mol/mol)  $O_2$ : $TiCl_4$  in argon (99% by volume) in a 1/8-in-I.D. tube heated to 973-1273 K. Pratsinis et al. [46] estimate an effective rate constant for the overall oxidation kinetics of  $TiCl_4$  vapour

$$k_{\text{eff}} = -\frac{\ln(C_o/C_i)}{t}, \quad (21)$$

assuming the reaction is first-order in  $TiCl_4$  with Arrhenius kinetics and where  $C_i$  and  $C_o$  are the measured inlet and outlet  $TiCl_4$  concentrations.  $t$  is the residence time in the isothermal zone of the reactor held at temperature  $T$ . The experiment was simulated using

the imposed temperature profile of Pratsinis et al. [46, Fig. 3] modelled by Akroyd et al. [1].

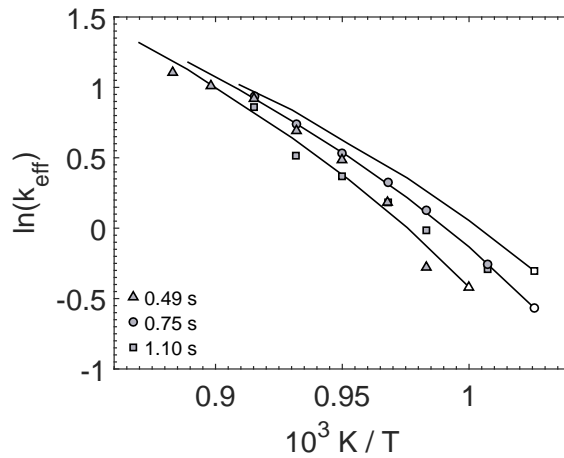


**Figure 6:** Arrhenius plot of the oxidation rate of  $\text{TiCl}_4$  at three different residence times. Black lines terminating in open symbols: fitted simulation results (4 runs with 8192 particles); Shaded symbols: Experimental data [46, Fig. 4].

Figure 6 shows good agreement between detailed particle model simulations with 8192 stochastic particles and the experimental results of Pratsinis et al. [46, Fig. 4]. The data are presented in the original form for easy comparison.

The surface growth rate was fitted with activation energy  $E_a = 60 \text{ kJ/mol}$  and pre-exponential factor  $A = 1340 \text{ m}^4/(\text{s} \cdot \text{mol})$  (see equation (4)). The fitted activation energy is in agreement with the theoretically calculated value ( $55 \pm 25 \text{ kJ/mol}$ ) of Shirley et al. [53].

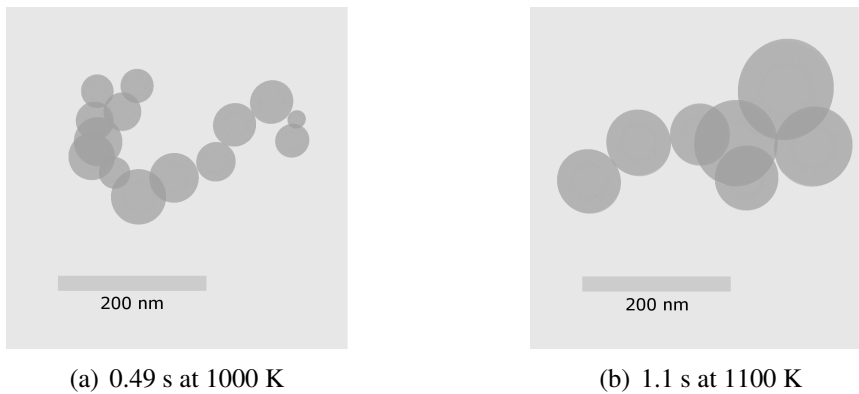


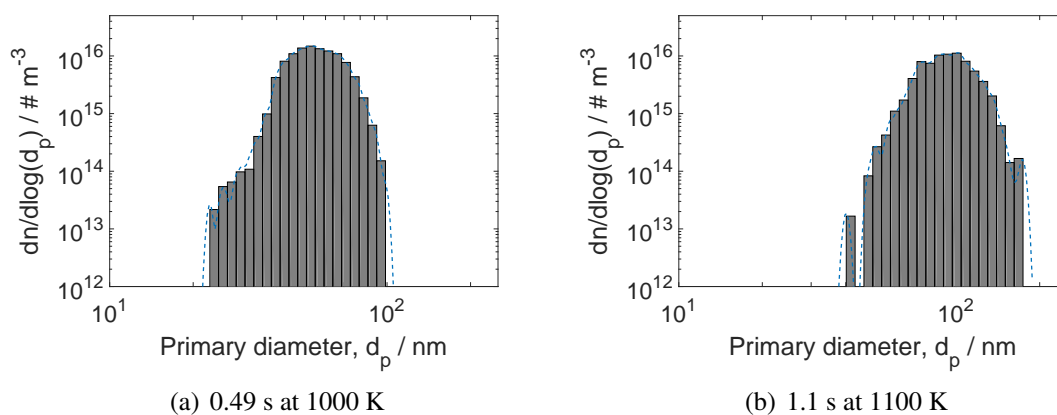
**Figure 7:** TEM style images of titania aggregates produced in the simulated hot wall reactor under different conditions. The visualisation does not depict the level of sintering between particles, however this information is captured by the model.

Simulation data is visualised in figure 7 in the form of TEM style images showing titania particles produced in the hot wall reactor under different residence times and temperatures. Aggregate particles produced over a longer residence time at higher temperature



(1.1 s at 1100 K shown in figure 7(b)) are composed of a smaller number of larger primaries than aggregates produced at a lower temperature and shorter residence time (0.49 s at 1000 K shown in figure 7(a)). This is clear from the primary diameter distribution (figure 8) and the distribution of the number of primaries per aggregate (figure 9).

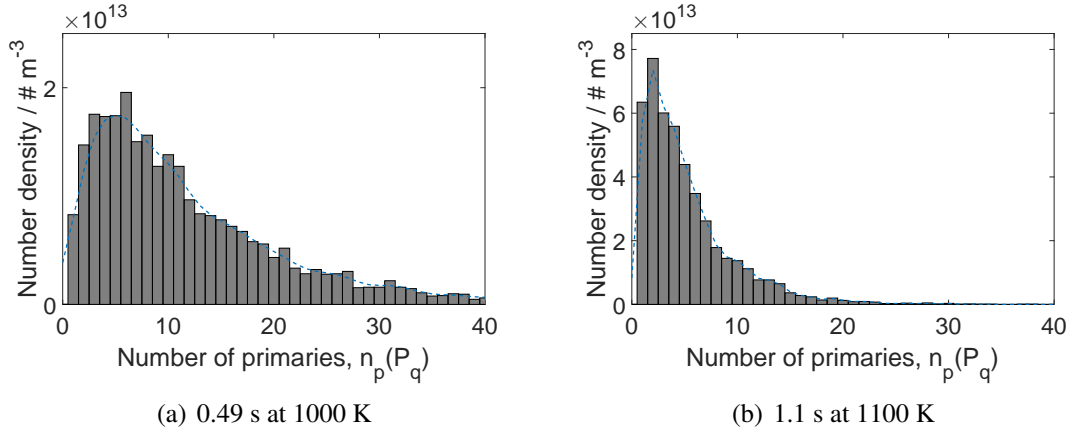
The difference in aggregate particle size is less pronounced. Figure 10 shows the distribution of particle collision diameters calculated as per Lavvas et al. [34]. The aggregate particle size is a function of the number of primary particles, their respective diameters, and the level of sintering between neighbours. This allows for aggregates of comparable size despite the different primary particle properties. The largest particles are of similar size under both sets of reactor conditions, but the distribution in figure 10(a) extends to smaller collision diameters. The smallest particles are composed of a single primary particle and the lower minimum value arises due to the smaller mean primary diameter.



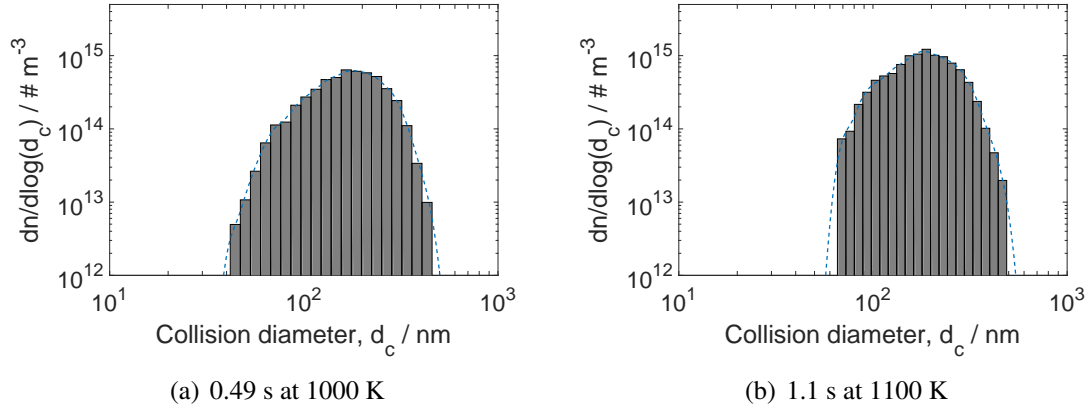
**Figure 8:** *Primary particle diameter distributions produced under different simulated reactor residence times and temperatures. The dashed line shows the Gaussian kernel density estimate.*

Figure 11 shows the distribution of neck radii. Up to 5% of necks were calculated to be in point contact ( $a_{ij} = 0$ ) and are not shown in the figure. These necks are considered to represent primaries bound by weak dispersion forces that have yet to begin sintering. Larger necks with well defined radii correspond to sintered primaries joined by strong chemical bonds.

We observe a bimodal distribution in both simulations with a peak residing at a radius of 0.01–0.1 nm: smaller than an atomic diameter. The overlapping spheres model permits the neck radius to take any positive value and does not account for quantization at very small length scales. Furthermore, molecular dynamics studies of sintering of nanometre sized titania particles show that the formation of an initial neck is very rapid, of the order of 10 picoseconds [8, 13, 30], whereas in this work sintering is treated as a continuous process with the same characteristic time at all stages.



**Figure 9:** *Distribution of the number of primaries per titania aggregate produced under different simulated reactor residence times and temperatures. The dashed line shows the Gaussian kernel density estimate.*



**Figure 10:** *Collision diameter distributions of titania aggregates produced under different simulated reactor residence times and temperatures. The dashed line shows the Gaussian kernel density estimate.*

## 4.2 Comparison of breakage models

The breakage models presented in section 3.2 were used to post-process the hot wall reactor simulation results of section 4.1 using algorithm 1. The results of post-processing the 0.49 s at 1000 K simulation are discussed here as a representative case because they display the general features of the different breakage models also observed in the other reactor simulations. Under the assumption that necks in point contact ( $a_{ij} = 0$ ) break apart easily we processed the data to break these necks prior to milling.

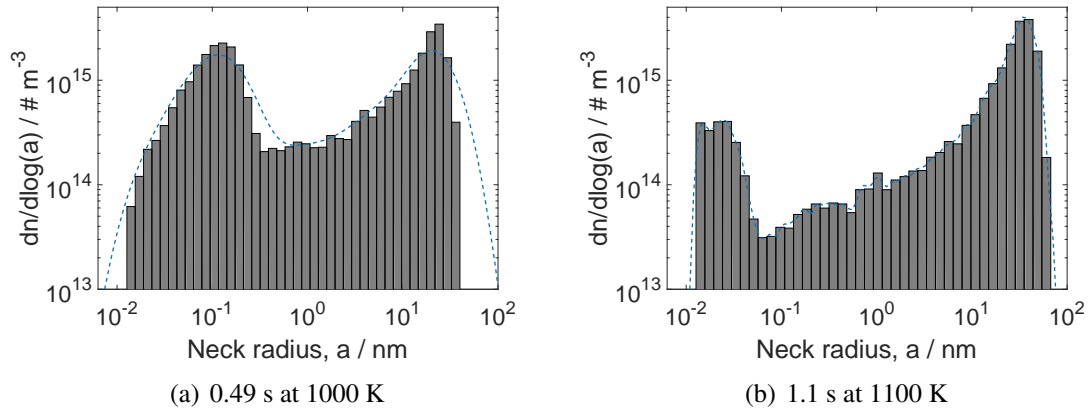


**Figure 11:** Neck radius distribution for titania aggregates produced in the simulated hot wall reactor under two different conditions. Necks with  $a_{ij} = 0$  are not shown. The dashed line shows the Gaussian kernel density estimate.

#### 4.2.1 Milling curves

Typically observed industrial milling curves (from Huntsman Pigments and Additives) are shown in figure 12. The volume weighted mean particle size is observed to decrease logarithmically over the period covered by the data. The width of the PSD as measured by the volume weighted geometric standard deviation (GSD) of particle size also exhibits logarithmic decay. The data set does not contain the initial particle size distribution nor the long time behaviour of particles under milling.

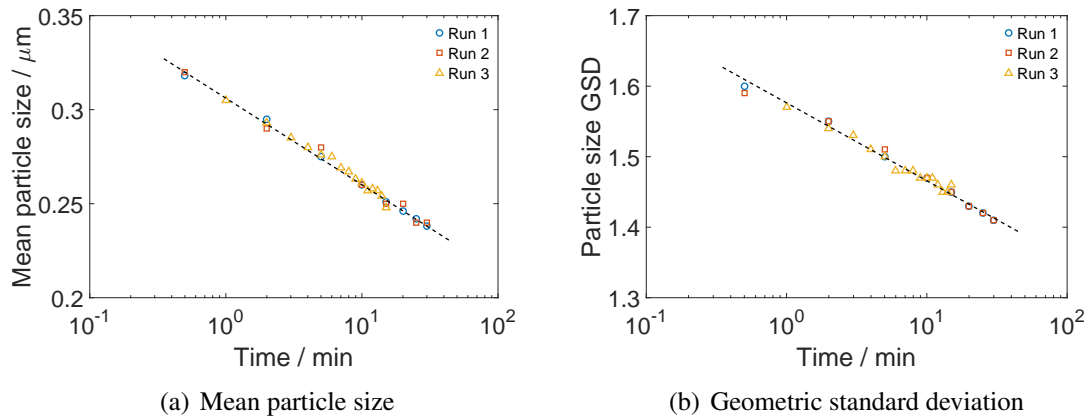


**Figure 12:** Experimental milling curves (Huntsman Pigments and Additives) show logarithmic decay in both the volume weighted mean particle size and geometric standard deviation. Dashed line added to guide the eye.

Figure 13 shows the corresponding simulated milling curves for the different breakage models. The time coordinate is non-dimensionalised by defining a characteristic time equal to the time taken for the mass weighted geometric mean collision diameter to fall

to 90% of its initial value. The mass weighted geometric mean (GM) and mass weighted GSD are given by

$$\ln(\text{GM}) = \frac{\sum_{q=1}^N m(P_q) \ln(d_c(P_q))}{\sum_{q=1}^N m(P_q)}, \quad (22)$$

$$\ln(\text{GSD}) = \sqrt{\frac{\sum_{q=1}^N m(P_q) [\ln(d_c(P_q)) - \ln(\text{GM})]^2}{\sum_{q=1}^N m(P_q)}}, \quad (23)$$

for  $N$  particles  $P_q$  each with mass  $m(P_q)$  and collision diameter  $d_c(P_q)$ .

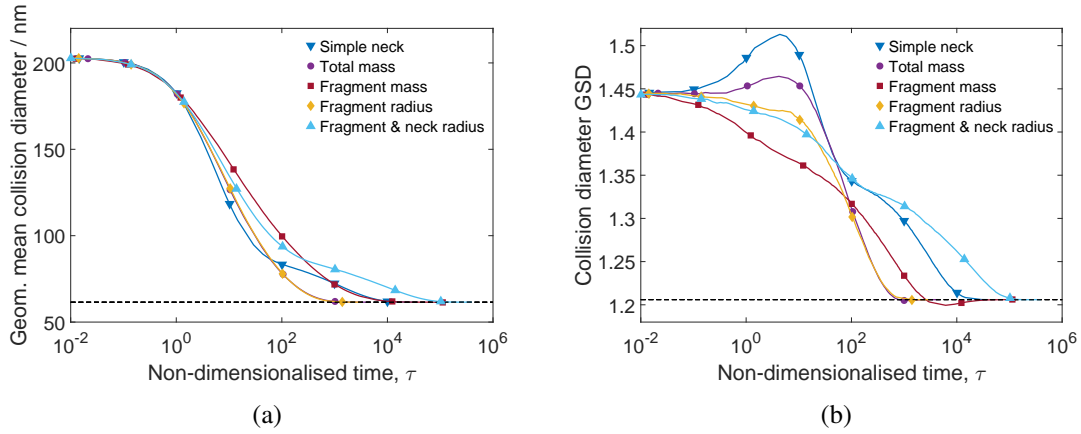


**Figure 13:** Milling curves for different breakage models obtained by post-processing hot wall reactor simulation results for the 0.49 s at 1000 K case. (a) shows the mass weighted geometric mean collision diameter and (b) the mass weighted geometric standard deviation in the collision diameter. The horizontal dashed line indicates the asymptotic value calculated from the primary particle distribution.

A value of -1 was selected for the exponent  $\alpha$  in the simple neck and the fragment radius and neck models yielding rates inversely proportional to the neck radius. A negative exponent implies that larger necks require greater stresses to break. More negative choices of  $\alpha$  introduce a long intermediate period during which the GM and GSD change very little. This is observed to small degree in the simple neck model ( $\alpha = -1$  case) in figure 13(b) where the gradient changes at around  $\tau = 100$ .

Figure 13(a) plots the mass weighted geometric mean collision diameter against non-dimensionalised time. All models exhibit an intermediate period of approximately logarithmic decay as seen in the experimental milling curves (figure 12). The total mass and fragment radius models have almost identical mean collision diameter curves. The simple neck and fragment and neck radius models show two distinct phases of size reduction characterised by different gradients. The change in gradient arises due to the bimodal nature of the neck size distribution. The first mode of small necks breaks first followed by the second mode of larger and stronger necks.

The GSD curves (figure 13(b)) offer a clearer way to differentiate between models. Most display an intermediate period of approximately logarithmic decay. An interesting feature is the initial increase in GSD seen in the total mass and simple neck models. Such an increase in the variance has been observed experimentally in the grinding of titanium dioxide [3]. This arises due to the formation of small fragments that cause a widening in the particle size distribution and can be seen in the mass weighted collision diameter distributions in figure 14. The distribution near the maximum GSD for the simple neck model ( $\tau = 4.4$  in figure 14(a)) is skewed with more mass density at smaller diameters contributing to a wider, lower peak. In comparison, the fragment and neck radius model in figure 14(b) maintains a more symmetric distribution due to a preference for symmetrical breakage events.

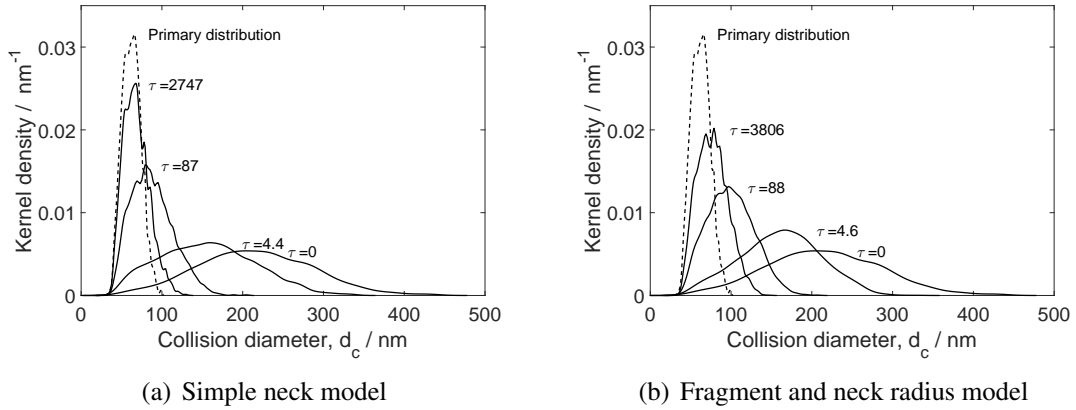


**Figure 14:** Mass weighted collision diameter distributions generated using a Gaussian kernel density estimate at different non-dimensionalised times for the 0.49 s at 1000 K reactor simulation post-processed with the (a) simple neck and (b) fragment and neck radius models.

#### 4.2.2 Comparison to a first order model

There are uncertainties around modelling the milling process, therefore models are fitted to experimental data in order to extract the milling kinetics and identify the breakage mechanism at work. The milling process can be described with a PBM and the size reduction behaviour is often adequately approximated by a first order exponential function over sufficiently short milling times [4, 21, 22, 59]. In this section we want to explore how the kinetics of our breakage models compare with a first order exponential model.

The cumulative form of the discrete population balance equation for batch milling is (following [4, 5])

$$\frac{dR_i}{dt} = -S_i R_i(t) + \sum_{j=1}^{i-1} (S_{j+1} B_{i,j+1} - S_j B_{i,j}) R_j(t), \quad (24)$$

with

$$R_i(t) = \sum_{j=1}^i w_j(t) \quad \text{and} \quad B_{i,j} = \sum_{k=i+1}^n b_{k,j}. \quad (25)$$

$R_i(t)$  is the cumulative oversize mass fraction of particles larger than size  $x_i$ .  $w_j$  is the mass fraction of particles in size class  $j$ , with  $w_1$  corresponding to the largest size class.  $S_i$ , the selection function, is the probability of breakage of particles in size class  $i$ .  $b_{k,j}$ , the breakage function, is the mass fraction of particles in class  $j$  that break to produce particles in size class  $k$ .

The approximate solution of Kapur [28], to first order in  $t$ , has the form

$$R_i(t) = R_i(0) \exp(G_i t). \quad (26)$$

and the selection function  $S_i$  can then be related to  $G_i$  [5]

$$S_i = -G_i. \quad (27)$$

Figure 15 presents the simulation results in the form  $R_i(\tau)/R_i(0)$  for nine size classes. The particle size,  $x_i$ , is the spherical equivalent diameter. The breakage models all display an early period of exponential decay consistent with a first order solution. Exponential curves with parameter  $G_i$  (equation (26)) were fitted to the simulation data in this period and are shown in figure 15 as dashed lines.

After the initial period of approximately exponential decay the curves begin to diverge. An approximate first order solution is therefore only appropriate over a short milling time up to  $\tau = 1$  to  $\tau = 5$ , depending on the model. However, we can compare the fitted values of  $G_i$  as a function of spherical equivalent diameter  $x_i$ , valid over the initial period, to typical selection functions reported in the literature.

The function  $G_i$  can often be represented by a power law in particle size [4, 25]

$$G_i = -ax_i^b. \quad (28)$$

Values of the exponent  $b$  observed for the milling of solid particles are typically close to unity [4, 22, 25]. A quadratic form for  $G_i$  has been reported for the milling of micrometer sized titanium dioxide [16]. Significantly larger values of  $b$  have been observed for alumina particles sintered at 1873 K (about 3) [25] and for the grinding of amorphous pre-mullite powder (3.18) [35]. Hennart et al. [22] show a power law dependence with exponent 6.5 for particles below 0.180  $\mu\text{m}$  in diameter when grinding a crystalline organic product limited by aggregation phenomena.

Figure 16 shows a power law fitting for the fitted values of  $G_i$  for the different models. The exponent ranges from 3.37 for the simple neck model to 7 in the case of the fragment mass model. These are considerably larger than typically observed values for grinding and closer to values reported for highly sintered aggregates and small particles approaching a grinding limit.

### 4.2.3 Choice of breakage model

While it is difficult to exclude models based on the qualitative comparison of milling curves, the current work illustrates the different features produced by each model, particularly with regard to the GSD and evolution of the PSD. Of the five breakage models

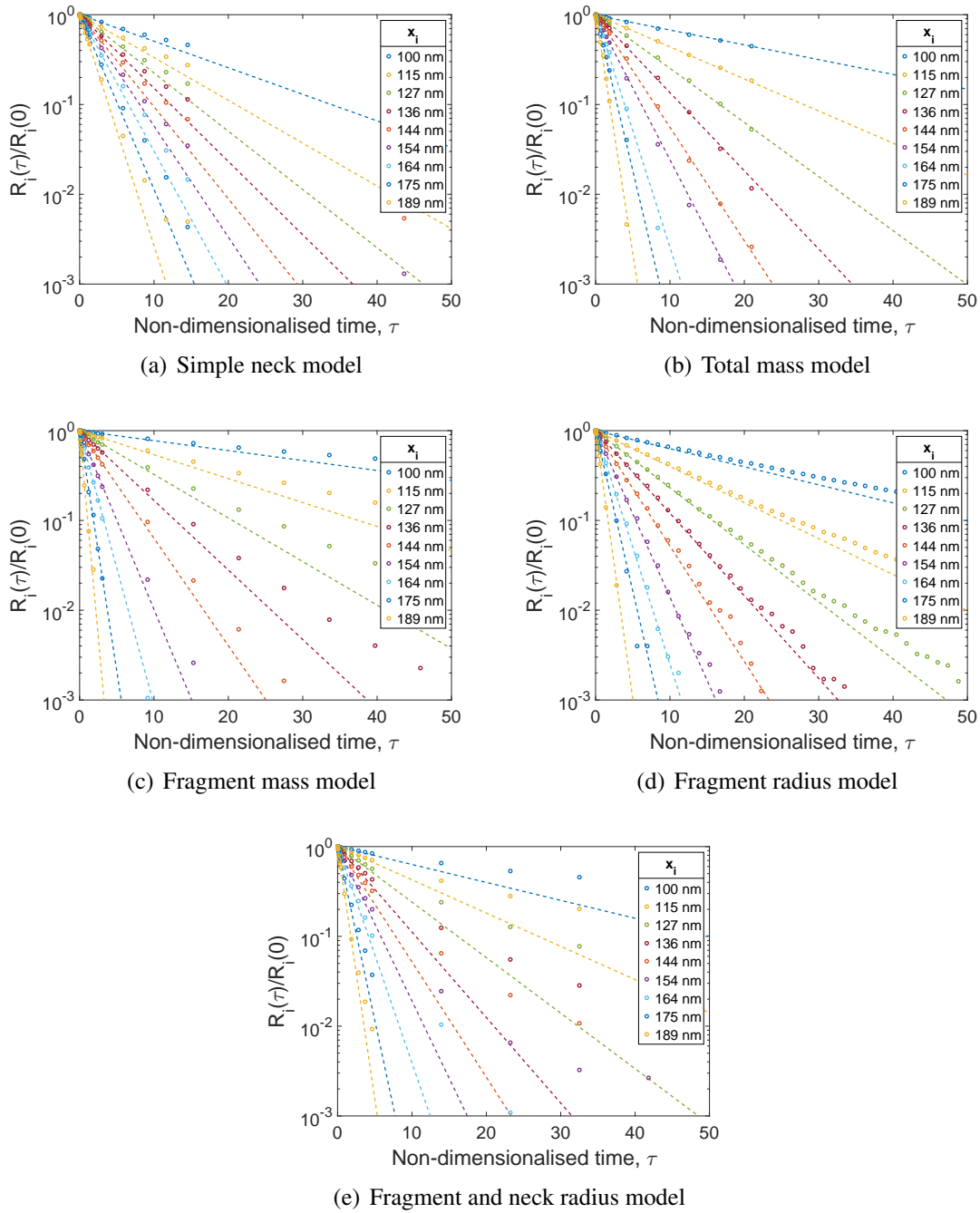


**Figure 15:** Normalised cumulative mass fraction overshize against non-dimensionalised time for nine spherical equivalent particle diameters up to time  $\tau = 50$ . Symbols: simulation data; Dashed lines: exponential decay fitted to data at early times.

discussed here only the fragment and neck radius model considers the aggregate particle geometry as well as the neck strength. The dependence on aggregate geometry favours symmetrical breakage in a cleavage type mechanism. On the other hand, the neck size

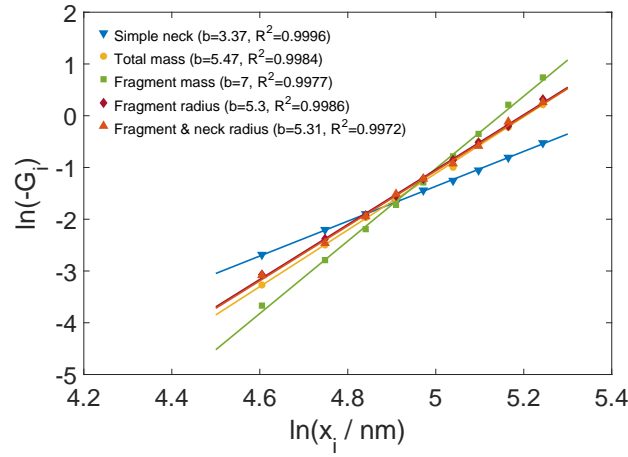


**Figure 16:** Fitted power law in spherical equivalent particle diameter for the different breakage models. The fitted exponent  $b$  and  $R^2$  value are shown in the legend.

dependence favours small necks allowing for cases of asymmetrical breakage near the particle extremities similar to an abrasion mechanism. Since the model accounts for the detailed particle morphology it serves as good candidate for further study.

### 4.3 Effect of reactor conditions on milling curves

The fragment and neck radius model was applied to simulations of the hot wall reactor experiment under different conditions. Results are shown in figure 17. The time coordinate was non-dimensionalised for all cases using the characteristic time calculated for the 0.49 s at 1000 K case allowing for better comparison along the time axis.

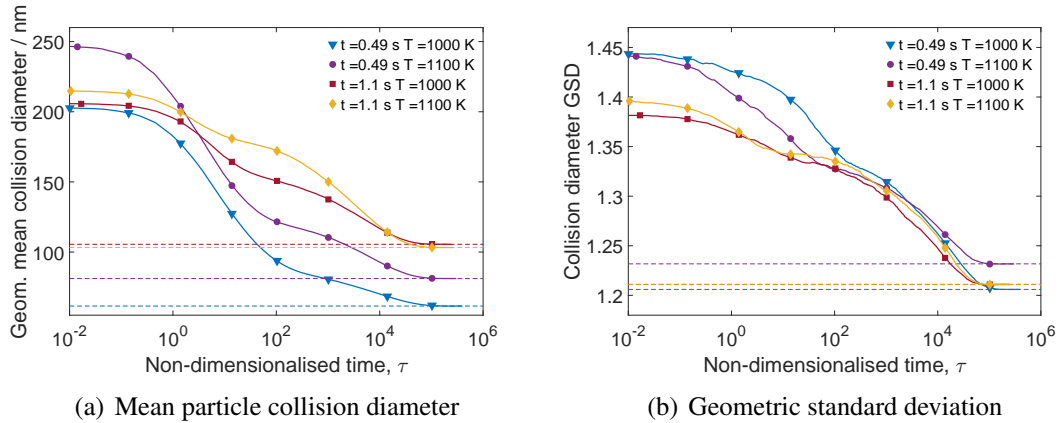


**Figure 17:** Milling curves for the fragment and neck radius model obtained by post-processing hot wall reactor simulation results under different conditions. The horizontal dashed line shows the asymptotic value calculated from the primary particle distribution.



All simulations take approximately the same time to reach an asymptotic state. Two phases of approximately logarithmic decay, characterised by different gradients, are observed due to the bimodal neck size distribution. In the 1.1 s residence time simulations the first phase is not as well defined. The longer residence time results show a slower decrease in the mean particle size and a smaller total change. Both 0.49 s simulations display a rapid first phase of size reduction followed by a slower second phase.

The model shows that particles synthesised over a short reactor residence time are milled faster and reduced to a smaller asymptotic size. The GSD has a higher initial value but catches up with the longer residence time models over the first phase of size reduction. The effect of temperature, within the range used in this study, is less pronounced.

## 5 Conclusions

A detailed population balance was used to model the formation of titanium dioxide particles in a hot wall reactor and validated against the experiment of Pratsinis et al. [46]. The detailed particle type space was shown to resolve morphological differences between particles produced under different reactor conditions.

Breakage models were developed that utilise the information captured by the detailed particle model and used as a post-process to simulate the milling of  $\text{TiO}_2$  particles produced in the hot wall reactor simulations. The milling curves exhibited features consistent with experimental observations. The chosen breakage model accounts for the fractal structure of the aggregate particles as well as the size of necks between neighbouring primaries. Application of this milling model to particles produced under different residence times and temperatures showed that the model is sensitive to the reactor conditions under which the  $\text{TiO}_2$  particles were synthesised.

Further work is needed to compare the model against experimental results and fit the breakage rate constant. This would first require simulation of the reactor conditions under which the experimental  $\text{TiO}_2$  particles are produced to allow subsequent comparison to experimental milling data. There is also scope to improve the sintering and neck size models given the observed limitations of the current model at low levels of sintering.

## Acknowledgements

This project is partly funded by the National Research Foundation (NRF), Prime Minister's Office, Singapore under its Campus for Research Excellence and Technological Enterprise (CREATE) programme. The authors would like to thank Huntsman Pigments and Additives for financial support.

## References

- [1] J. Akroyd, A. J. Smith, R. Shirley, L. R. McGlashan, and M. Kraft. A coupled CFD-population balance approach for nanoparticle synthesis in turbulent reacting flows. *Chem. Eng. Sci.*, 66:3792–3805, 2011. doi:10.1016/j.ces.2011.05.006.
- [2] H. Bel Fadhel and C. Frances. Wet batch grinding of alumina hydrate in a stirred bead mill. *Powder Technol.*, 119:257–268, 2001. doi:10.1016/S0032-5910(01)00266-2.
- [3] H. Bel Fadhel, C. Frances, and A. Mamourian. Investigations on ultra-fine grinding of titanium dioxide in a stirred media mill. *Powder Technol.*, 105:362–373, 1999. doi:10.1016/S0032-5910(99)00160-6.
- [4] H. Berthiaux, D. Heitzmann, and J. A. Dodds. Validation of a model of a stirred bead mill by comparing results obtained in batch and continuous mode grinding. *Int. J. Miner. Process.*, 44-45:653–661, 1996. doi:10.1016/0301-7516(95)00073-9.
- [5] H. Berthiaux, C. Varinot, and J. Dodds. Approximate calculation of breakage parameters from batch grinding tests. *Chem. Eng. Sci.*, 51:4509–4516, 1996. doi:10.1016/0009-2509(96)00275-8.
- [6] E. Bilgili and B. Scarlett. Population balance modeling of non-linear effects in milling processes. *Powder Technol.*, 153:59–71, 2005. doi:10.1016/j.powtec.2005.02.005.
- [7] E. Bilgili, R. Hamey, and B. Scarlett. Nano-milling of pigment agglomerates using a wet stirred media mill: Elucidation of the kinetics and breakage mechanisms. *Chem. Eng. Sci.*, 61:149–157, 2006. doi:10.1016/j.ces.2004.11.063.
- [8] B. Buesser, A. J. Gröhn, and S. E. Pratsinis. Sintering rate and mechanism of TiO<sub>2</sub> nanoparticles by molecular dynamics. *J. Phys. Chem. C*, 115:11030–11035, 2011. doi:10.1021/jp2032302.
- [9] M. Celnik, R. Patterson, M. Kraft, and W. Wagner. Coupling a stochastic soot population balance to gas-phase chemistry using operator splitting. *Combust. Flame*, 148:158–176, 2007. doi:10.1016/j.combustflame.2006.10.007.
- [10] M. Celnik, A. Raj, R. West, R. Patterson, and M. Kraft. Aromatic site description of soot particles. *Combust. Flame*, 155:161–180, 2008. doi:10.1016/j.combustflame.2008.04.011.
- [11] M. S. Celnik, M. Sander, A. Raj, R. H. West, and M. Kraft. Modelling soot formation in a premixed flame using an aromatic-site soot model and an improved oxidation rate. *Proc. Combust. Inst.*, 32:639–646, 2009. doi:10.1016/j.proci.2008.06.062.
- [12] D. Chen, Z. Zainuddin, E. Yapp, J. Akroyd, S. Mosbach, and M. Kraft. A fully coupled simulation of pah and soot growth with a population balance model. *Proc. Combust. Inst.*, 34:1827–1835, 2013. doi:10.1016/j.proci.2012.06.089.

- [13] D. R. Collins, W. Smith, N. M. Harrison, and T. R. Forester. Molecular dynamics study of the high temperature fusion of TiO<sub>2</sub> nanoclusters. *J. Mater. Chem.*, 7:2543–2546, 1997. doi:10.1039/A704673A.
- [14] A. Eibeck and W. Wagner. An efficient stochastic algorithm for studying coagulation dynamics and gelation phenomena. *SIAM J. Sci. Comput.*, 22:802–821, 2000. doi:10.1137/S1064827599353488.
- [15] B. Epstein. Logarithmico-normal distribution in breakage of solids. *Ind. Eng. Chem.*, 40:2289–2291, 1948. doi:10.1021/ie50468a014.
- [16] C. Frances. On modelling of submicronic wet milling processes in bead mills. *Powder Technol.*, 143-144:253–263, 2004. doi:10.1016/j.powtec.2004.04.018.
- [17] U. Gesenhues. Substructure of titanium dioxide agglomerates from dry ball-milling experiments. *J. Nanopart. Res.*, 1:223–234, 1999. doi:10.1023/A:1010097429732.
- [18] R. N. Ghoshtagore. Mechanism of heterogeneous deposition of thin film rutile. *J. Electrochem. Soc.*, 117:529–534, 1970. doi:10.1149/1.2407561.
- [19] M. Goodson and M. Kraft. An efficient stochastic algorithm for simulating nano-particle dynamics. *J. Comput. Phys.*, 183:210–232, 2002. doi:10.1006/jcph.2002.7192.
- [20] M. C. Heine and S. E. Pratsinis. Polydispersity of primary particles in agglomerates made by coagulation and sintering. *J. Aerosol Sci.*, 38:17–38, 2007. doi:10.1016/j.jaerosci.2006.09.005.
- [21] S. L. A. Hennart, W. J. Wildeboer, P. van Hee, and G. M. H. Meesters. Identification of the grinding mechanisms and their origin in a stirred ball mill using population balances. *Chem. Eng. Sci.*, 64:4123–4130, 2009. doi:10.1016/j.ces.2009.06.031.
- [22] S. L. A. Hennart, P. van Hee, V. Drouet, M. C. Domingues, W. J. Wildeboer, and G. M. H. Meesters. Characterization and modeling of a sub-micron milling process limited by agglomeration phenomena. *Chem. Eng. Sci.*, 71:484–495, 2012. doi:10.1016/j.ces.2011.11.010.
- [23] R. Hogg. Breakage mechanisms and mill performance in ultrafine grinding. *Powder Technol.*, 105:135–140, 1999. doi:10.1016/S0032-5910(99)00128-X.
- [24] R. Hogg and H. Cho. A review of breakage behavior in fine grinding by stirred-media milling. *KONA Powder Part. J.*, 18:9–19, 2000. doi:10.14356/kona.2000007.
- [25] R. Hogg, A. J. Dynys, and H. Cho. Fine grinding of aggregated powders. *Powder Technol.*, 122:122–128, 2002. doi:10.1016/S0032-5910(01)00407-7.
- [26] M. Inkyo, T. Tahara, T. Iwaki, F. Iskandar, C. J. Hogan Jr., and K. Okuyama. Experimental investigation of nanoparticle dispersion by beads milling with centrifugal bead separation. *J. Colloid Interface Sci.*, 304:535–540, 2006. doi:10.1016/j.jcis.2006.09.021.

- [27] S. Jeon, T. Thajudeen, and C. J. H. Jr. Evaluation of nanoparticle aggregate morphology during wet milling. *Powder Technol.*, 272:75 – 84, 2015. doi:<http://dx.doi.org/10.1016/j.powtec.2014.11.039>.
- [28] P. C. Kapur. Kinetics of batch grinding. Part B: An approximate solution to the grinding equation. *Trans. AIME*, 247:309–313, 1970.
- [29] A. Kobata, K. Kusakabe, and S. Morooka. Growth and transformation of TiO<sub>2</sub> crystallites in aerosol reactor. *AIChE J.*, 37:347–359, 1991. doi:[10.1002/aic.690370305](https://doi.org/10.1002/aic.690370305).
- [30] V. N. Koparde and P. T. Cummings. Molecular dynamics simulation of titanium dioxide nanoparticle sintering. *J. Phys. Chem. B*, 109:24280–24287, 2005. doi:[10.1021/jp054667p](https://doi.org/10.1021/jp054667p).
- [31] A. Kwade. Wet comminution in stirred media mills – research and its practical application. *Powder Technol.*, 105:14–20, 1999. doi:[10.1016/S0032-5910\(99\)00113-8](https://doi.org/10.1016/S0032-5910(99)00113-8).
- [32] A. Kwade and J. Schwedes. Breaking characteristics of different materials and their effect on stress intensity and stress number in stirred media mills. *Powder Technol.*, 122:109–121, 2002. doi:[10.1016/S0032-5910\(01\)00406-5](https://doi.org/10.1016/S0032-5910(01)00406-5).
- [33] A. Kwade, L. Blecher, and J. Schwedes. Motion and stress intensity of grinding beads in a stirred media mill. Part 2: Stress intensity and its effect on comminution. *Powder Technol.*, 86:69–76, 1996. doi:[10.1016/0032-5910\(95\)03039-5](https://doi.org/10.1016/0032-5910(95)03039-5).
- [34] P. Lavvas, M. Sander, M. Kraft, and H. Imanaka. Surface chemistry and particle shape. Processes for the evolution of aerosols in Titan’s atmosphere. *Astrophys. J.*, 728:80, 2011. doi:[10.1088/0004-637X/728/2/80](https://doi.org/10.1088/0004-637X/728/2/80).
- [35] G. Matijašić and S. Kurajica. Grinding kinetics of amorphous powder obtained by sol-gel process. *Powder Technol.*, 197:165–169, 2010. doi:[10.1016/j.powtec.2009.09.010](https://doi.org/10.1016/j.powtec.2009.09.010).
- [36] M. Mehta, Y. Sung, V. Raman, and R. O. Fox. Multiscale modeling of TiO<sub>2</sub> nanoparticle production in flame reactors: Effect of chemical mechanism. *Ind. Eng. Chem. Res.*, 49:10663–10673, 2010. doi:[10.1021/ie100560h](https://doi.org/10.1021/ie100560h).
- [37] M. Mehta, R. O. Fox, and P. Pepiot. Reduced chemical kinetics for the modeling of TiO<sub>2</sub> nanoparticle synthesis in flame reactors. *Ind. Eng. Chem. Res.*, 54:5407–5415, 2015. doi:[10.1021/acs.iecr.5b00130](https://doi.org/10.1021/acs.iecr.5b00130).
- [38] W. J. Menz and M. Kraft. The suitability of particle models in capturing aggregate structure and polydispersity. *Aerosol Sci. Technol.*, 47:734–745, 2013. doi:[10.1080/02786826.2013.788244](https://doi.org/10.1080/02786826.2013.788244).
- [39] N. Morgan, C. Wells, M. Kraft, and W. Wagner. Modelling nanoparticle dynamics: Coagulation, sintering, particle inception and surface growth. *Combust. Theor. Model.*, 9:449–461, 2005. doi:[10.1080/13647830500277183](https://doi.org/10.1080/13647830500277183).

- [40] N. Morgan, C. G. Wells, M. J. Goodson, M. Kraft, and W. Wagner. A new numerical approach for the simulation of the growth of inorganic nanoparticles. *J. Comput. Phys.*, 211:638–658, 2006. doi:10.1016/j.jcp.2005.04.027.
- [41] N. M. Morgan, R. I. A. Patterson, and M. Kraft. Modes of neck growth in nanoparticle aggregates. *Combust. Flame*, 152:272–275, 2008. doi:10.1016/j.combustflame.2007.08.007.
- [42] K. Ohenoja, M. Illikainen, and J. Niinimäki. Effect of operational parameters and stress energies on the particle size distribution of TiO<sub>2</sub> pigment in stirred media milling. *Powder Technol.*, 234:91–96, 2013. doi:10.1016/j.powtec.2012.09.038.
- [43] R. I. A. Patterson, J. Singh, M. Balthasar, M. Kraft, and J. R. Norris. The linear process deferment algorithm: A new technique for solving population balance equations. *SIAM J. Sci. Comput.*, 28:303–320, 2006. doi:10.1137/040618953.
- [44] R. I. A. Patterson, J. Singh, M. Balthasar, M. Kraft, and W. Wagner. Extending stochastic soot simulation to higher pressures. *Combust. Flame*, 145:638–642, 2006. doi:10.1016/j.combustflame.2006.02.005.
- [45] S. E. Pratsinis and P. T. Spicer. Competition between gas phase and surface oxidation of TiCl<sub>4</sub> during synthesis of TiO<sub>2</sub> particles. *Chem. Eng. Sci.*, 53:1861–1868, 1998. doi:10.1016/S0009-2509(98)00026-8.
- [46] S. E. Pratsinis, H. Bai, P. Biswas, M. Frenklach, and S. V. R. Mastrangelo. Kinetics of titanium (IV) chloride oxidation. *J. Am. Ceram. Soc.*, 73:2158–2162, 1990. doi:10.1111/j.1151-2916.1990.tb05295.x.
- [47] S. Redner. Fragmentation. In H. J. Herrmann and S. Roux, editors, *Statistical models for the fracture of disordered media*, pages 321–348. Elsevier, Amsterdam, 1990. doi:10.1016/B978-0-444-88551-7.50021-5.
- [48] M. Sander, R. H. West, M. S. Celnik, and M. Kraft. A detailed model for the sintering of polydispersed nanoparticle agglomerates. *Aerosol Sci. Technol.*, 43:978–989, 2009. doi:10.1080/02786820903092416.
- [49] M. Sander, R. I. A. Patterson, A. Braumann, A. Raj, and M. Kraft. Developing the PAH-PP soot particle model using process informatics and uncertainty propagation. *Proc. Combust. Inst.*, 33:675–683, 2011. doi:10.1016/j.proci.2010.06.156.
- [50] S. Shekar, W. J. Menz, A. J. Smith, M. Kraft, and W. Wagner. On a multivariate population balance model to describe the structure and composition of silica nanoparticles. *Comput. Chem. Eng.*, 43:130–147, 2012. doi:10.1016/j.compchemeng.2012.04.010.
- [51] S. Shekar, A. J. Smith, W. J. Menz, M. Sander, and M. Kraft. A multidimensional population balance model to describe the aerosol synthesis of silica nanoparticles. *J. Aerosol Sci.*, 44:83–98, 2012. doi:10.1016/j.jaerosci.2011.09.004.

- [52] R. Shirley, Y. Liu, T. S. Totton, R. H. West, and M. Kraft. First-principles thermochemistry for the combustion of a  $\text{TiCl}_4$  and  $\text{AlCl}_3$  mixture. *J. Phys. Chem. A*, 113:13790–13796, 2009. doi:10.1021/jp905244w.
- [53] R. Shirley, J. Akroyd, L. A. Miller, O. R. Inderwildi, U. Riedel, and M. Kraft. Theoretical insights into the surface growth of rutile  $\text{TiO}_2$ . *Combust. Flame*, 158:1868–1876, 2011. doi:10.1016/j.combustflame.2011.06.007.
- [54] M. Sommer, F. Stenger, W. Peukert, and N. J. Wagner. Agglomeration and breakage of nanoparticles in stirred media mills – a comparison of different methods and models. *Chem. Eng. Sci.*, 61:135–148, 2006. doi:10.1016/j.ces.2004.12.057.
- [55] T. S. Totton, R. Shirley, and M. Kraft. First-principles thermochemistry for the combustion in a methane flame. *Proc. Combust. Inst.*, 33:493–500, 2011. doi:10.1016/j.proci.2010.05.011.
- [56] S. Tsantilis and S. E. Pratsinis. Narrowing the size distribution of aerosol-made titania by surface growth and coagulation. *J. Aerosol Sci.*, 35:405–420, 2004. doi:10.1016/j.jaerosci.2003.09.006.
- [57] S. Tsantilis, H. K. Kammler, and S. E. Pratsinis. Population balance modeling of flame synthesis of titania nanoparticles. *Chem. Eng. Sci.*, 57:2139–2156, 2002. doi:10.1016/S0009-2509(02)00107-0.
- [58] C. Varinot, S. Hiltgun, M.-N. Pons, and J. Dodds. Identification of the fragmentation mechanisms in wet-phase fine grinding in a stirred bead mill. *Chem. Eng. Sci.*, 52:3605–3612, 1997. doi:10.1016/S0009-2509(97)89693-5.
- [59] C. Varinot, H. Berthiaux, and J. Dodds. Prediction of the product size distribution in associations of stirred bead mills. *Powder Technol.*, 105:228–236, 1999. doi:10.1016/S0032-5910(99)00142-4.
- [60] E. W. Weisstein. Sphere-sphere intersection. From MathWorld - A Wolfram Web Resource, accessed 15 Oct 2015. URL <http://mathworld.wolfram.com/Sphere-SphereIntersection.html>.
- [61] E. W. Weisstein. Spherical cap. From MathWorld - A Wolfram Web Resource, accessed 15 Oct 2015. URL <http://mathworld.wolfram.com/SphericalCap.html>.
- [62] C. G. Wells, N. M. Morgan, M. Kraft, and W. Wagner. A new method for calculating the diameters of partially-sintered nanoparticles and its effect on simulated particle properties. *Chem. Eng. Sci.*, 61:158–166, 2006. doi:10.1016/j.ces.2005.01.048.
- [63] R. H. West, G. J. O. Beran, W. H. Green, and M. Kraft. First-principles thermochemistry for the production of  $\text{TiO}_2$  from  $\text{TiCl}_4$ . *J. Phys. Chem. A*, 111:3560–3565, 2007. doi:10.1021/jp0661950.
- [64] R. H. West, M. S. Celnik, O. R. Inderwildi, M. Kraft, G. J. O. Beran, and W. H. Green. Toward a comprehensive model of the synthesis of  $\text{TiO}_2$  particles from  $\text{TiCl}_4$ . *Ind. Eng. Chem. Res.*, 46:6147–6156, 2007. doi:10.1021/ie0706414.

- [65] R. H. West, R. A. Shirley, M. Kraft, C. F. Goldsmith, and W. H. Green. A detailed kinetic model for combustion synthesis of titania from  $\text{TiCl}_4$ . *Combust. Flame*, 156: 1764–1770, 2009. doi:[10.1016/j.combustflame.2009.04.011](https://doi.org/10.1016/j.combustflame.2009.04.011).
- [66] Y. Xiong and S. E. Pratsinis. Formation of agglomerate particles by coagulation and sintering—Part I. A two-dimensional solution of the population balance equation. *J. Aerosol Sci.*, 24:283–300, 1993. doi:[10.1016/0021-8502\(93\)90003-R](https://doi.org/10.1016/0021-8502(93)90003-R).
- [67] E. K. Yapp, R. I. Patterson, J. Akroyd, S. Mosbach, E. M. Adkins, J. H. Miller, and M. Kraft. Numerical simulation and parametric sensitivity study of optical band gap in a laminar co-flow ethylene diffusion flame. *Combust. Flame*, 167:320 – 334, 2016. doi:<http://dx.doi.org/10.1016/j.combustflame.2016.01.033>.
- [68] E. K. Y. Yapp, D. Chen, J. Akroyd, S. Mosbach, M. Kraft, J. Camacho, and H. Wang. Numerical simulation and parametric sensitivity study of particle size distributions in a burner-stabilised stagnation flame. *Combust. Flame*, 162:2569–2581, 2015. doi:[10.1016/j.combustflame.2015.03.006](https://doi.org/10.1016/j.combustflame.2015.03.006).